Volume 33 | Number 8 | August 2018 | Pages 1277–1404

JAAS

Journal of Analytical Atomic Spectrometry

rsc.li/jaas

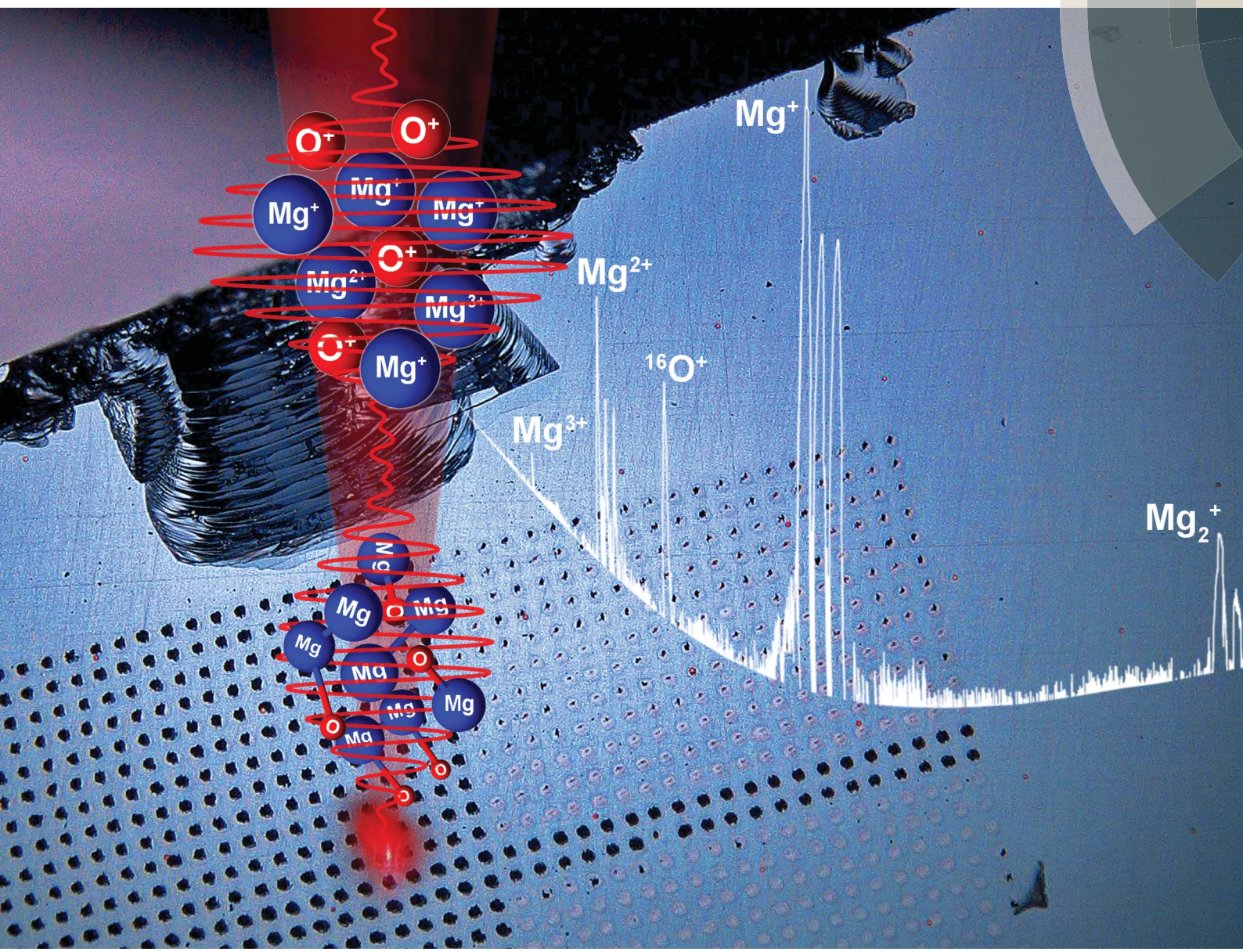

ISSN 0267-9477

ROYAL SOCIETY OF CHEMISTRY

PAPER

M. Tulej *et al.*

Mass spectrometric analysis of the Mg plasma produced by double-pulse femtosecond laser irradiation

JAAS

PAPER

View Article Online
View Journal | View Issue

Check for updates

Cite this: J. Anal. At. Spectrom., 2018, 33, 1292

Mass spectrometric analysis of the Mg plasma produced by double-pulse femtosecond laser irradiation

M. Tulej, *[a] R. Wiesendanger, [a] A. Riedo, [ab] G. Knopp[c] and P. Wurz [a]

The capabilities of a double-pulse (DP) femtosecond (fs) laser ablation of solid materials as an ion source for application in a miniature Laser ionisation time-of-flight Mass Spectrometer (LMS) system designed for space research are investigated. The studies are conducted by irradiating a high-purity Mg sample with sequences of two femtosecond laser pulses. The positively charged fraction of the Mg plasma is analysed as a function of the inter-pulse delay in the range from 0 to 300 ps and for pulse energies in the range from 0.2 to 1 μJ. The DP ablation studies with both pulses of similar energy show a Mg^+ ion yield enhancement within the inter-pulse delay range from 1 to 35 ps near the ablation energy threshold (AET) and from 1 to ~300 ps if larger pulse energies are applied for the first ablation pulse. For the same total energies but different individual pulse energies, Mg^+ ions are produced more efficiently if the weaker pulse is applied first. The analyses of Mg^+, multiple-charged Mg and Mg cluster ion yields as a function of the inter-pulse delay and the pulse energies improve the understanding of the ablation mechanism and add some insights into the dynamics of the Mg-surface melting and cooling phases, thermal characteristics of the expanding plasma plume and atomic/cluster ion production mechanisms. By applying sufficiently high DP energies > (0.3 + 0.3) μJ the clusters which are likely produced in the initial ablation phase at the surface can be decomposed effectively in the heated plasma plume. Moreover, by tuning the inter-pulse delay one can also efficiently suppress the neutral-ion reactions in post-plasma chemistry. Our studies show that the DP femtosecond laser ablation ion source can improve the mass spectrometric analysis of solid samples by increasing the ion yield of atomic ions and reducing the abundance of cluster ions. This can improve the quantitative analyses of elements and their isotopes by increasing signal-to-noise ratios and reducing isobaric interferents arising from cluster ions. The current DP studies are conducted successfully with pulse energies lower than 1 μJ, which is sufficiently low to be realised in a compact, lightweight system using fibre technology based lasers, suitable for *in situ* space applications.

Received 5th February 2018
Accepted 18th May 2018

DOI: 10.1039/c8ja00036k

rsc.li/jaas

Published on 18 May 2018. Downloaded on 8/13/2018 3:18:34 PM.

Introduction

Laser ablation of solid materials using short laser pulses has attracted considerable interest in the last two decades in various fields of application, ranging from pulsed laser deposition,[1] laser material processing and micromachining,[2,3] nanoparticle synthesis[4,5] thin film technology[6,7] and chemical analysis of solids by femtosecond laser-induced breakdown spectroscopy (fs-LIBS),[8] femtosecond laser ablation inductively-coupled plasma mass spectrometry (fs-LA-ICP-MS) also including a multi-collector system typically applied in the isotope analysis (fs-LA-MC-ICP-MS)[9,10] and femtosecond laser ablation/ionisation mass spectrometry (fs-LIMS).[11,12] Low heat transfer from the irradiated surface, reduced melting depth and no laser-plasma interaction due to a short laser pulse duration are found to be advantages in these applications yielding high precision in material processing with reduction of the heat affected zone (HAZ), low material damage and reduction of elemental fractionation effects.[8,11–17]

More accurate energy accumulation in solid materials is achieved by using a pair of femtosecond pulses which are applied with a sufficiently long inter-pulse delay. The application of femtosecond pulse trains and bursts with specific pulse energies and separated from each other by several nanoseconds leads to further improvements in laser micro-fabrication.[18] For shorter delays between laser pulses, the second pulse can readily interact with the expanding plasma plume. By transferring the laser energy into different stages of the expanding plasma plume one can achieve a certain control over the surface ablation process and physical and chemical properties of the

[a]Physics Institute, Space Research and Planetary Sciences, University of Bern, Sidlerstrasse 5, 3012 Bern, Switzerland. E-mail: marek.tulej@space.unibe.ch
[b]Sackler Laboratory for Astrophysics, Leiden Observatory, Leiden University, Niels Bohrweg 2, 2333 CA Leiden, The Netherlands
[c]SwissFEL Photonics Group, Paul Scherrer Institute, 5232 Villigen PSI, Switzerland

This journal is © The Royal Society of Chemistry 2018

Published on 18 May 2018. Downloaded on 8/13/2018 3:18:34 PM.

plasma plume.[19,20] The DP ablation method is found to be useful in controlling the characteristics of laser-induced craters improving depth profiling but also producing smoother crater shapes compared to that produced by single-pulse (SP) ablation.[21,22] Also improvements of stoichiometric atom detection efficiency in chemical analysis while using a fs-DP ion source were reported in LIBS investigations.[23,24] In typical DP-LIBS application using nanosecond laser sources the apparent emission signal increase is attributed to either heating of the sample surface by the first pulse, atmospheric effects with generation of shock waves, pressure gradients at the plasma location or a coupling of the second laser pulse into the plasma plume produced by the first pulse. The latter effect leads to an additional excitation of the plasma and an enhancement of plasma emission intensity.[24] However, by using fs-DP ablation the emission signal increase is found to be dependent on the inter-pulse delay. In one of the LIBS studies conducted on metallic targets in ambient air, three inter-pulse delay regimes were defined by combining analyses of crater depth and emission signal enhancement.[25] For the delays between the pulses smaller than 1 ps no emission signal enhancement was observed. For the pulse delays from 1 ps to 10 ps the LIBS signal was observed to increase and the ablation depth was observed to decrease which was accounted for by a partial shielding of the target sample. For the inter-pulse delays larger than 10 ps the target was observed to be completely shielded. A highly reproducible, large emission signal enhancement by a factor of 3 to 10 was observed in LIBS measurements by applying UV femtosecond laser beams.[24] The measured signal enhancement remained constant in the entire inter-pulse delay range from 50 to 1000 ps.

The combined experimental and modelling studies conducted in the last two decades have delivered a relatively detailed mechanism of DP ablation on various solid state materials.[10,20,26–30] It has been established that for the inter-pulse delays shorter than 1 ps, DP ablation is similar to that of SP ablation with the pulse energy equal to the sum of the energies of the individual pulses applied in the DP method.[31,32] At these delays, the laser radiation is absorbed by the conduction band electrons *via* the inverse bremsstrahlung within the optical penetration depth of a few nm. Due to the small duration of a femtosecond laser pulse compared with the electron-phonon relaxation time, which is <10 ps for most of the metals, non-equilibrium energy transport is expected to the surface material. The electrons are heated first to high temperatures whereas the lattice still remains at low temperature. After the electron thermalisation in the conduction band, they diffuse deeper into sample surface. Sufficiently hot electrons and electrons produced by multiphoton absorption can overcome the potential barrier and leave the surface. These electrons can pull out ions from the surface and further ionise them by impact ionisation.[17,33,34] This induces a breakdown of the interrogated volume followed by ejection of atomic clusters following a Coulomb explosion and appearance of the plasma. Due to ultrafast and isochoric heating, a rapid temperature increase followed by an adiabatic expansion of the ejected volume and condensation of the ejecta. One defines several intermediate thermodynamic pathways with decrease of pulse energy including vaporisation, fragmentation, phase explosion and spallation.[10,35–37]

In laser ablation of metals, the plasma plume is formed typically after a few ps. The second pulse is found to be useful to deliver diagnostics of the ablation conditions because of its good coupling to the plasma plume. Dedicated plasma diagnostic experiments have shown that in laser ablation of metals the atomic ions are produced within 1 to 100 ps after the ablation pulse.[7,22,38] It was argued that while using DP ablation, within the delays in the range from 1 to 5 ps, the second laser pulse influences still an electron distribution at the surface that is not in equilibrium with the lattice and the metallic ion yield starts to rise slowly within this inter-pulse delay range. At delays larger than >5 ps the cloud of atoms produced by the first pulse can be found near the surface region and the plasma plume density is sufficiently high that efficient absorption of laser radiation through atomic excitation and inverse bremsstrahlung followed by plasma heating can produce large ion yields.[23,39]

The molecular dynamics simulation and hydrodynamic modelling were applied to interpret the experimental findings.[22,27,38,40–46] Modelling studies of ablation of metals deliver detailed analysis of relaxation dynamics at the ablation spot. The irradiated lattice while relaxing induces high tensile stresses on the surface layer with a bulk melting of a superheated layer with formation of pressure–temperature profiles.[47] A thin liquid ablation layer separated by a layer of melt undergoes an explosion followed by the formation and expansion of a plasma plume with fragmentation, atomisation and formation of a vapour of atoms and clusters. Two distinct ablation plumes including a fast atomic plume (<20% of the total ablated mass and <1% fraction of atomic ions) and slower plume containing nanolayers (nanoparticles), which form a major part of the ablated mass, are produced.[48–50] It is generally accepted that the initial plume is highly charged, non-thermal species, while the second, slower component is composed of singly- or doubly-charged ions. Near the ablation threshold, this second component could also include clusters and nanoparticles. These two ablation plumes were observed in imaging experiments and are predicted in the modelling studies.[34,35] Hydrodynamic modelling explained formally that the interaction of the pressure waves produced by the first pulse on the sample surface and second pulse on the expanding plasma plume suppresses possible effects of the second pulse on the ablation of the surface material.[32,51] Also more advanced investigations including laser ablation by temporally modified laser pulse intensity profiles (pulse-shaping method) proved to be even more efficient in controlling plasma temperature and ablation rates.[23,32,51,52] Using arbitrary pulse sequences (referred to as temporal pulse shaping) one can achieve the required optimization and full control over the plasma parameters *e.g.*, arbitrary sequences are produced in this method at the expense of temporal (bandwidth-limited) spread.[53]

The aim of the current investigations is to examine the DP femtosecond laser ablation as a potential ion source in analyses of solid materials by our miniature time-of-flight mass spectrometer (TOF-MS) developed for space research.[54] The fully

Published on 18 May 2018. Downloaded on 8/13/2018 3:18:34 PM.

developed and deployed instrument will be used to conduct investigation of elemental and isotope composition of planetary rocks and soils. Accurate and sensitive chemical analyses of planetary rocks and soils are the forefront in space research. While from the elemental analysis one can conclude on the origin and evolution of planetary materials, isotope measurements can provide *e.g.* formation ages or evidence on biosignatures from the analysis of isotope fractionation effects of bio-relevant elements.[55,56] The analysis of major and minor elements with concentrations down to the fraction of per cent can deliver the mineralogical composition of planetary materials.[57] The measurements of trace elements abundant down to the ppm level are planned to be conducted on planetary materials to investigate times of their formation.[58] In searches for life on other planets, analysis of putative fossilised materials will be of considerable interest.[59–61] For these studies, isotope accuracies have to be at the per mille level which can be achieved currently using our instrument for species concentrations down to 10 parts per million (ppm).[12,58,59] Nevertheless, isobaric interference due to the presence of cluster ions can significantly affect the accuracy and precision of our measurements.

The developments in the last two decades in laser ionisation mass spectrometry (LIMS) including instrumental ion transmission improvements, modification of the experimental setup and coupling of an fs-laser ion source with a mass analyser have opened new perspectives in the application of this analytical technique for quantitative elemental and isotope analysis.[12,62,63] Further improvements to a laser ion source seem to be possible either by increasing the atomic ion production and/or reducing unwanted contribution from cluster ions. In laboratory practice, cluster ion abundances can be controlled to some extent (*e.g.*, by increasing laser irradiance and modification of the experimental setup and ion detection method).[64] However, these methods cannot be implemented in our miniature LIMS system. The DP ion source is promising as an alternative method in this context. The small size, low mass and minimal power consumption for the instrument can be maintained (considering application of a femtosecond fibre laser) and at the same time the quantitative performance of the system can be improved by increasing the apparent atomic ion signal and decreasing the cluster ion concentration minimising isobaric interference.

Our miniature space-prototype LIMS system was developed for the BepiColombo lander in 2003.[54] A more advanced instrumental package was presented for the Marco Polo-R sample return mission to an asteroid.[59] So far, one miniature LIMS instrument, the LAZMA instrument, has flown on the Phobos Sample Return mission.[65] The LAZMA instrument is accepted for the Luna Resource mission to the Moon (2022).

In our present investigations we analyse the chemical composition of an Mg plasma using our miniature reflectron-type mass analyser (LMS). The choice of Mg as a sample matrix is driven by simplicity, so that the improvements due to the DP method can be readily measured and quantified. More advanced analyses of standard research materials are planned in the near future to establish the quantitative performance of the instrument while coupled with a DP ion source.

In the current contribution we study the performance of DP ablation as a function of pulse energies and inter-pulse delays. We analyse temporally resolved Mg^+, multiple-charged Mg^+ and Mg^+ cluster ion yields to establish conditions for an optimal ion production efficiency and minimisation of cluster abundances in the analysed ion beam. Clusters are frequently observed in laser ablation mass spectrometric studies contributing to isobaric interference.[63,66] So far, reducing the cluster abundances in the plasma produced by SP ablation has proved to be challenging.[11,67] The analyses of temporally resolved DP ion yield curves are conducted in addition to characterise the ablation dynamics, thermal state of the expanding plasma and variation of the chemical composition of the plasma plume. The preliminary results of these studies are promising for the future application of the DP ion source to sensitive chemical analysis of solids; by tuning the energy and delay of the second pulse one can readily increase atomic ion yields and efficiently decompose Mg clusters into atoms.

Experimental

Materials

A high-grade Mg foil (4×4 mm^2, thickness of 0.5 mm, purity 99.9%, Goodfellow, UK) and Mg alloy AZ31 (Mg96/Al3/Zn1, Goodfellow) were used as received. To clean and condition the sample surface prior to measurements, 5000 laser shots (SP laser ablation, 0.4 μJ per pulse) were applied before each measurement.

Experimental setup

The ablation studies are conducted by focusing the fs-laser radiation to a spot size close to 10 μm in diameter onto a high-purity Mg sample surface and subsequent analysis using a miniature laser ionisation mass spectrometer system. The measurement vacuum chamber is kept under ultra-high vacuum conditions at 5×10^{-8} mbar. The construction, operation principles, and data acquisition method of our LMS system are discussed in detail in previous publications.[12,57,58,68–70] Here, only a short description will be given including description of our new optical setup for a DP laser ablation ion source (Fig. 1). For the construction of the DP system, the output of an fs-laser (Chirped Pulse Amplified (CPA) Clark-MXR: $t \sim 180$ fs, $\lambda = 775$ nm, laser pulse repetition rate $\leq$ 1 kHz, maximum pulse energy: 1 mJ, and s-polarisation) is used. After changing the s-polarised beam into a p-polarised beam with a half-wave plate, the beam was sent to a home-made interferometer (Fig. 1). The beam is first split into two beams of equal pulse energy (beam splitter #1). One of the beams (pulse 1) passes an optical delay line composed of the dielectric mirror M1 and a retroreflector placed on a motorised micro-translation stage (Zaber, GMP, Switzerland) allowing control of the delay times between the two pulses. The second beam (pulse 2) is directed into the delay line with a fixed path length arranged by the set of dielectric mirrors, M2–M6. Both laser beams are subsequently re-combined with high precision at beam splitter #2. In the current studies the micro-translation

 This journal is © The Royal Society of Chemistry 2018

Published on 18 May 2018. Downloaded on 8/13/2018 3:18:34 PM.

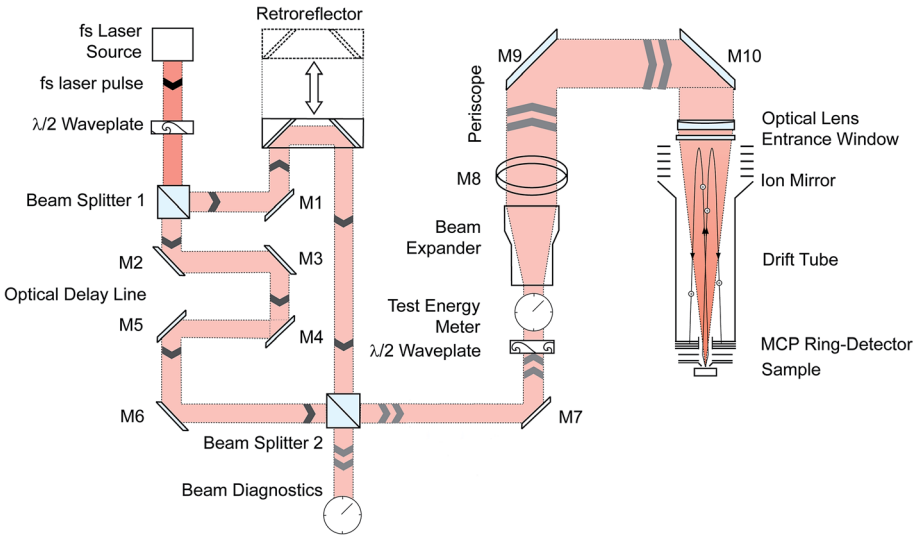

Fig. 1 Schematic of the DP fs-laser ion source combined with a miniature mass spectrometer (see text for more details).

stage is moved over the distance of ~100 mm, for obtaining the inter-pulse delay range from −300 to +300 ps. With the translation distance of 50 μm, a time delay of ~300 fs is achieved. The total energy of both beams is controlled by a half-wave plate and polariser system (variable attenuator, Newport) positioned behind the beam splitter #2 (Fig. 1). For a few measurements beams of two different energies were used. This was achieved by inserting reflective neutral density filters in the beam path of pulse 2.

The spatially overlapped laser beams (Gaussian profiles) are expanded to a beam diameter of 35 mm by a beam expander and guided into the vacuum chamber by a periscope system. In the vacuum chamber, the laser beams are focused by a doublet lens (f/250) to a spot size of about 10 μm in diameter on the sample surface. The spatial overlap of both beams is established to the accuracy of about 2 μm by using an *in situ* microscope-camera system. The details of the construction and operation of the microscope-camera system used for the verification of the overlap are discussed in a recent publication.[71]

The exact temporal overlap of the laser beams is achieved by tuning the micro-translational stage to observe an interference pattern produced by two beams behind beam splitter #2. The optical setup also allows for on-line beam diagnostics such as light polarisation analysis and pulse energy measurements and measurements of the 387.5 nm emission of a BBO crystal which radiates at maximum intensity at temporal overlap once the precise zero delay position is reached. The spot sizes of the propagating beam profiles were also examined by a beam profiler camera near the focal plane.

The sample is placed on an *xyz* translation stage, and positioned at the laser focus located about 0.5 mm from the entrance to the mass spectrometer. The laser irradiates the sample perpendicularly to its surface and initiates the ablation and ionisation processes. The ions extracted from the plasma plume are confined, accelerated and focused by the ion optical system allowing only positively charged species to enter the mass analyser. Mass separation occurs on the field-free drift paths of the mass spectrometer and the ions are recorded by a micro-strip multi-channel-plate detector system (chevron configuration).[72] A typical measurement is initiated by custom-made software controlling the laser operation, the sample position, the linear translation stage of the retroreflector, and the data acquisition system. The collected time-of-flight spectra are converted into mass spectra and integrated by the specifically prepared software.[69,73] The time-of-flight spectrum is measured by collecting ions of elements or clusters and oxides arrived at the detector within a certain time. The mass peak intensity is measured in the units of electrons per ns. The time-of-flight spectrum is then converted into a mass spectrum using the following equation:

$$M(T) = A(T + T_0)^2$$

where $M(T)$ is the mass/charge and A and T_0 are fit constants.

The observed ion signal (Fig. 2–7) is obtained by the integration of the relevant mass peaks in the time-of-flight spectrum and is represented in the units of electrons. The MCP gain close to 10^6 is typically applied and the number of the spectra accumulated in each measurement is described below.

Measurements

The mass spectra of the plasma are collected by applying sequences of 5000 laser shots on each surface location for a range of conditions.

(1) The SP and DP ions produced in the Mg plasma are obtained in the pulse energy range from 0.2 to 1.0 μJ. The DP ion measurements are performed for the inter-pulse delay of 20 ps at which the maximum of Mg^+ ion intensity is observed.

(2) The measurements of ions produced in the Mg plasma as a function of the inter-pulse delay are conducted for delays from −300 to +300 ps, with a time resolution of about 300 fs. Each measurement was conducted on a fresh surface location and the spectra were collected from 2000 locations for each campaign.

Published on 18 May 2018. Downloaded on 8/13/2018 3:18:34 PM.

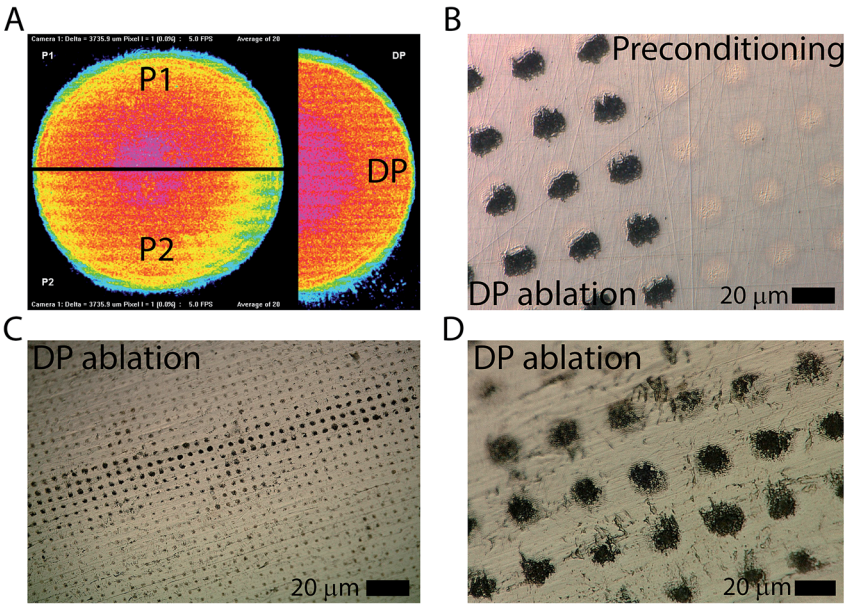

Fig. 2 (A) The laser beam profiles measured by a beam profile imager outside the focal point; P1, P2, and DP are the beam profiles of pulse 1, pulse 2, and double pulse, respectively; (B) typical images of the preconditioned surface by applying 5000 laser shots (right side) and after laser ablation studies; (C) the crater pattern obtained after the DP laser ablation while varying the inter-pulse delay between the pulses. Dark spots in the central part of the image are the craters made for inter-pulse delays from −15 to +15 ps (inter-pulse delay between near craters is ∼300 fs). Less pronounced crater spots are made at larger inter-pulse delays. (D) Close-up image of a few craters from the central part showing more details of the crater shapes.

(3) The mass spectra presented in Fig. 9 were obtained by the accumulation of 5000 single-shot mass spectra.

Laser beam profiles and crater images

Prior to the DP ablation measurements laser beam diagnostic studies were performed. The laser beam profiles for pulse 1 and pulse 2 were measured to be Gaussian. In addition, the beam profile of the overlapped beams at the focussing location was measured to ensure that they are overlapped and of equal intensity pattern (DP image). The temporal pulse shape was measured as well, yielding a pulse duration of ∼190 fs at full width half maximum (FWHM). The beam overlap could also be controlled independently during the measurement by means of the *in situ* microscope-camera system by analysing the laser ablation craters. Fig. 2B presents the image of the preconditioned surface (right side) and the laser crater obtained under the laser ablation conditions. The preconditioned areas do not show craters but ripples can be readily observed. In Fig. 2C, a surface with the crater pattern obtained after DP ablation as a function of the inter-pulse delay is shown. For the delays in the range from ∼15 ps to +15 ps the craters are deeper while for the other delays the ablation of the surface is less pronounced. This is due to plasma shielding effects for longer delays applied (see text in the Discussion section).

Results

SP measurements of Mg^+, multiple-charged Mg ions, and Mg cluster ions as a function of pulse energy

The mass spectrometric measurements of the SP plasma composition reveal the presence of Mg^+, multiple-charged Mg ions, and Mg cluster ions. The dependence of the ion as a function of pulse energy is depicted in Fig. 3. The Mg^+ ion signal increases linearly for the pulse energies larger than 0.30 μJ.

The ablation energy threshold (AET) of 0.30 ± 0.07 μJ is obtained by using a linear fit to the Mg^+ ion signal curve. A small Mg^+ ion signal is also detected for the pulse energies lower than

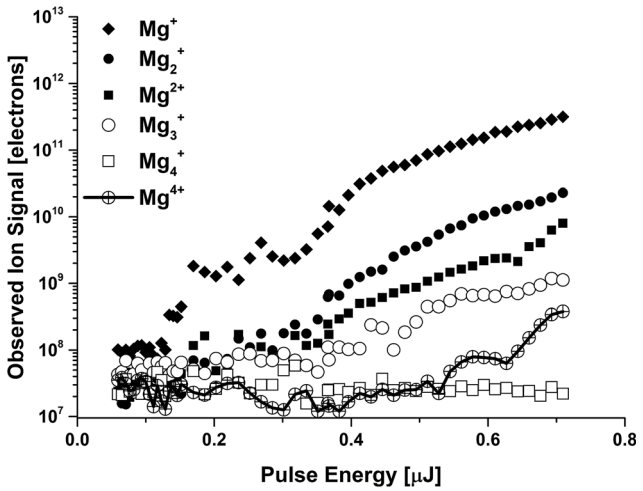

Fig. 3 The SP ablation measurements of Mg^+, Mg^{2+}, and Mg cluster ions as a function of pulse energy. The Mg^+ ion signal is observed for pulse energies larger than 0.3 μJ and the signals of multiple-charged ions Mg^{2+} and Mg^{4+} – for the pulse energy larger than 0.30 and 0.50 μJ, respectively. In the range of applied pulse energies an increase of the Mg cluster ion signal correlates well with the Mg^+ ion yield increase.

This journal is © The Royal Society of Chemistry 2018

Published on 18 May 2018. Downloaded on 8/13/2018 3:18:34 PM.

0.30 μJ but is not well correlated with the pulse energy increase. The Mg^{2+} and Mg^{4+} ions are measured for laser pulse energies larger than 0.40 and 0.50 μJ, respectively. The study also yields the detection of various Mg_x clusters and Mg_xO_y oxide ions where $x = 1$–4 and $y = 0$–3. The latter are produced due to the ablation of an oxidation layer in the upper most Mg target sample. An increase of the Mg_2^+ ion signal correlates well with an increase of the Mg^+ ion signal but the Mg_3 cluster signal increases somewhat slower. The threshold ablation fluence value, $F_{thr} \approx 130 \pm 60$ mJ cm^{-2}, is derived using the AET value and considering the crater sizes for the near threshold ablation energies scaling down to AET (crater diameter ~10 μm). In the estimation the surface reflectivity of $R = 0.5$ is assumed. This value is close to the ablation threshold fluence measured by a similar method for other metal samples.[74] Nevertheless, the threshold energy is determined from the mass spectra obtained by accumulation of 5000 individual mass spectra taken from the preconditioned surface with 5000 laser shots (see Fig. 2B). Hence, the unique dependence on the thermal and dynamical properties of materials, which is typically reflected from the one-shot ablation, is lost and the ion yield is likely affected by the history of prior laser shots on the sampled spot (*e.g.*, laser-induced periodic surface structures, LIPSS, ripples).[75] This initial laser irradiation of the surface changes surface optical properties and can readily increase surface absorptivity and decrease surface reflectance. The detection of the Mg^+ ions below the ablation threshold energy can be explained by surface changes by laser preconditioning.

Dependence of the Mg^+ ion yield on the inter-pulse delay

Guided by the results of the SP ablation studies, the pulse energies below and above AET are applied to investigate the DP Mg^+ ion signal enhancement as a function of the inter-pulse delay. Fig. 4 depicts the Mg^+ ion signal curves measured with pulse energies of 0.28 μJ (2 × 0.14 μJ), 0.70 μJ (2 × 0.35 μJ) and 0.86 μJ (2 × 0.43 μJ). The measurements with the lowest pulse energy close to AET show a Mg^+ ion signal enhancement in the relatively narrow inter-pulse delay range from 1 to 35 ps either when pulse 1 is applied first (negative delay) or when pulse 2 is applied first (positive delay). Similarly, symmetric Mg^+ signal enhancement curves are measured for the total pulse energy larger than AET, but the Mg^+ ion signal enhancement is observed now in a broader inter-pulse delay range from 1 to 300 ps. The Mg^+ ions are also measured for the nearly overlapping pulses with inter-pulse delays in the range from 0 to 1 ps. For temporally overlapped pulses, constructive and destructive interference occurs affecting Mg^+ ion production. For pulse energies much larger than AET the Mg^+ ion signal is observed to be comparable with the SP Mg^+ ion signal. We observed the Mg^+ ion signal enhancement for the inter-pulse delay of 20 ps close to 20 times compared to the Mg^+ ion signal produced by nearly overlapped pulses or SP ablation while applying pulse energies in the range from 0.30 to 0.70 μJ. For the pulse energies larger than AET, a Mg^+ ion signal enhancement is observed for the inter-pulse delays close to −150 ps and somehow less pronounced – for the delays close to +150 ps. The ion signal increase at these delays can be induced either by coincidental overlap of pre- or post-pulses of one laser beam with the main pulse of the second laser beam. The pre- and post-pulses can be produced near the main laser pulse but their intensities are typically more than 100 times lower compared to the intensity of the main laser pulse. These pulses are Fresnel reflections in optical elements or a radiation leakage out of the regenerative amplifier cavity (more details in ref. 8, p. 92). Typically, these pulses can be suppressed efficiently by adjusting the position of the Pockels cell. With our adjustments we could reduce pulse amplitudes but could not remove them entirely.

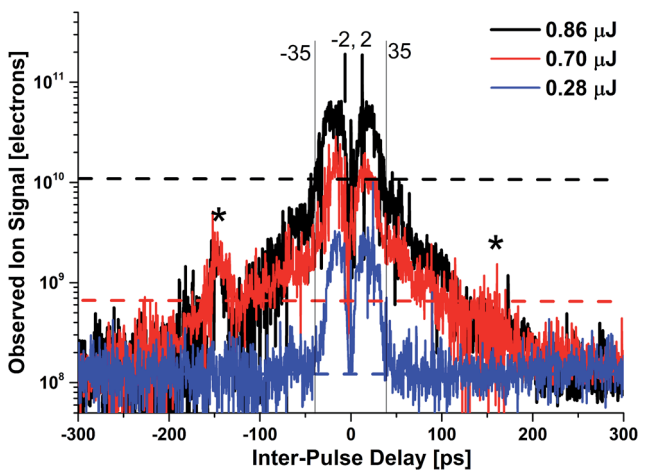

Fig. 4 The Mg^+ ion signal produced by a DP laser ablation source (both pulses have a similar pulse energy) as a function of the inter-pulse delay. The ion signal enhancement is observed for the inter-pulse delays between 2 and 35 ps with a maximal signal enhancement for the inter-pulse delay of 20 ps. For the delays from −1 to 1 ps, the Mg^+ ion signal increases similarly to that observed for SP ablation of the same total pulse energy.

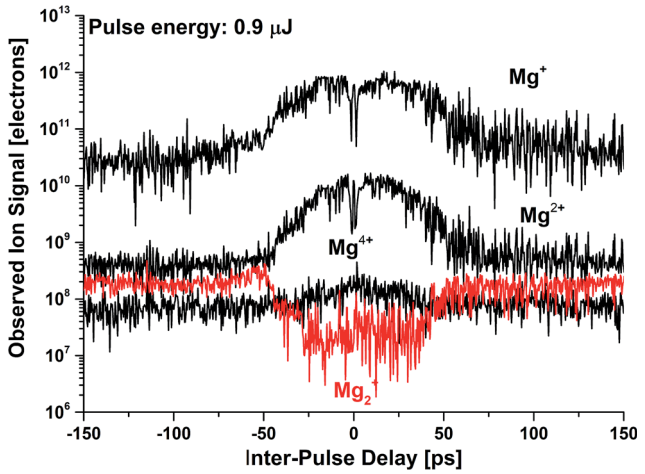

Fig. 5 The comparison between the signals of Mg^+, Mg^{2+}, Mg^{4+} and Mg_2^+ cluster ions measured for various inter-pulse delays. The multiple-charged Mg ion signals increase in the delay ranges from −50 to −1 ps and from +1 to +50 ps. Maxima of these signals are measured for the inter-pulse delay close to 20 ps. The Mg_2^+ cluster ion signal is observed to increase in the range from 50 to 75 ps and to decrease for the inter-pulse delays from −50 to −1 ps and from 1 to 50 ps.

Published on 18 May 2018. Downloaded on 8/13/2018 3:18:34 PM.

Fig. 5 depicts the signals of Mg^+, multiple-charged Mg^{2+} and Mg^{4+}, and Mg_2^+ cluster ions measured as a function of the inter-pulse delay for the total pulse energy of 0.9 μJ (2 × 0.45 μJ). Individual pulse energies are larger than the threshold ablation energy. The Mg^+ ion signal enhancement is observed in the delay range from −1 to −300 ps and from +1 to +300 ps. The Mg^+ ion signal measured for the inter-pulse delays from −1 to 1 ps is observed to be only a few times lower than that measured for the delay of 20 ps. The measurements show that the Mg^{2+} ion signal is enhanced for delays from −50 to +50 ps with the signal maximum for the inter-pulse delay of −20 and +20 ps. The Mg^{4+} ion signal enhancement is relatively small and occurs in the delay range −30 to +30 ps. The cluster ion signal changes differently. The Mg_2^+ cluster ion signal enhancement is observed for delays in the range from −75 to −50 ps and from +50 to +75 ps followed by its decrease in the range from −50 to −1 and from +1 to +50 ps, respectively. The measurements show that by applying sufficiently high pulse energies clusters can readily decompose in the plasma plume. The Mg_2^+ ion signal reaches a minimal value for the inter-pulse delays ranging from −30 to +30 ps.

Fig. 6 depicts the DP Mg^+ ion signal produced by the laser pulses of different energies in the inter-pulse delay range from −150 to +150 ps. When pulse 1 of lower energy (pulse 1 = 0.38 μJ) is applied first the Mg^+ ion yield is larger (see the part of the graph for the negative delays). For the reversed laser pulse configuration, the Mg^+ ion signal enhancement is readily lower (see the part of the graph for the positive delays). The Mg^+ ion signal enhancement in the positive delay range (pulse 2 applied first) is smaller but is observed in a broader inter-pulse delay range. The maximum signal enhancement is measured for the delays close to 20 ps, similarly, to the case when equal pulse energies are applied. In the negative delay range the signal enhancement of the Mg^{2+} ion and the signal decrease of the Mg_2^+ cluster ion are observed in the range from −1 to −30 ps. For the positive inter-pulse delays the signal of Mg_2^+ increases readily and there is almost no signal enhancement of the Mg^{2+} ion.

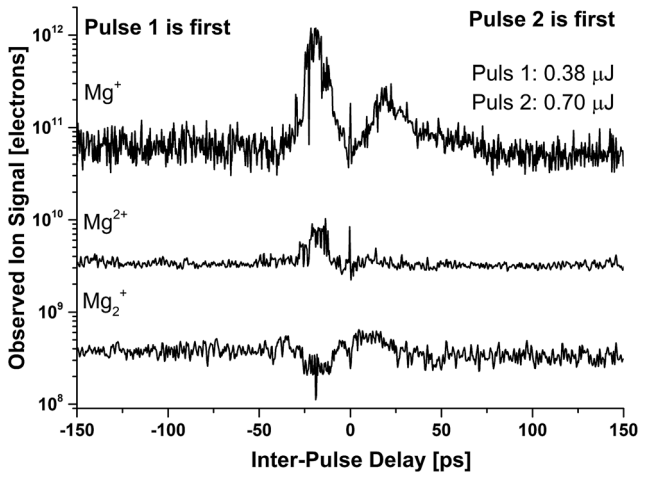

Fig. 6 The signal enhancements of Mg^+, Mg^{2+} and Mg_2^+ cluster ions as a function of the inter-pulse delay for different energies of pulse 1 and pulse 2. For the pulse 1 applied first (low pulse energy, negative delay) the Mg^+ ion signal enhancement is larger compared to the opposite pulse configuration. While the Mg^{2+} ion signal follows the changes of the Mg^+ ion signal the Mg_2^+ cluster signal decreases for the delays from −30 to −1 and increases for the positive delays from 1 to 50 ps.

Mg ion signal dependence on DP energy for an inter-pulse delay of 20 ps

Fig. 7 depicts the DP Mg^+ ion signal as a function of total pulse energy for the fixed inter-pulse delay of +20 ps (max. Mg^+ ion signal enhancement) (see Fig. 3). The rate of the Mg^+ ion signal enhancement is observed to increase somewhat faster in the energy range from 0.20 to 0.40 μJ than for the larger pulse energies. The Mg^{2+} and Mg^{4+} ion signals begin to increase for the pulse energies larger than ∼0.3 μJ and ∼0.6 μJ, respectively. The Mg_2^+ and Mg_3^+ cluster ion signals first increase in the pulse energy range from 0.2 to 0.5 μJ and decrease monotonically for larger pulse energies.

DP Mg^+ ion yield enhancement ratio relative to SP ion yield for various ablation energies

Fig. 8 depicts the DP Mg^+ ion signal enhancement relative to the SP Mg^+ ion signal. The ratio is calculated by dividing the DP ion signal values by the SP ion signal values measured for similar pulse energies. The measurements were conducted in the pulse range from 0.1 to 0.8 μJ. The DP Mg^+ ion signal enhancement is observed in the pulse energy range from 0.30 to 0.65 μJ reaching a value of about 20. For larger pulse energies the enhancement of the DP Mg^+ ion signal over the SP ion signal decreases reaching the value close to 10 for the pulse energy of 0.8 μJ. The measurements for larger pulse energies were not conducted.

Comparison of the mass spectra obtained by the SP and DP laser ablation

Fig. 9 depicts the mass spectra obtained in the measurements with SP (panel B) and DP ablation (equal pulse energies) (panel A) by applying a total pulse energy of 0.8 μJ for the inter-pulse

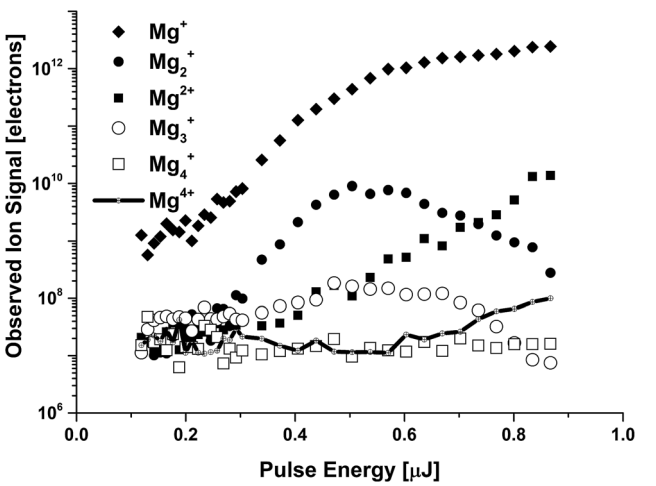

Fig. 7 The DP signals of Mg^+, Mg^{n+} and Mg_n^+ ions measured as a function of total pulse energy; pulse 1 and pulse 2 are delayed by 20 ps.

This journal is © The Royal Society of Chemistry 2018

Published on 18 May 2018. Downloaded on 8/13/2018 3:18:34 PM.

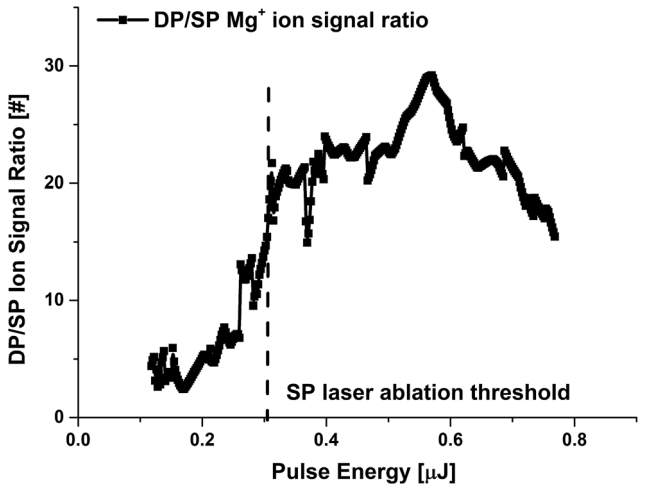

Fig. 8 The DP Mg^+ ion signal enhancement relative to the SP Mg^+ ion signal measured for a similar total energy in the energy range from 0.1 to 0.8 μJ.

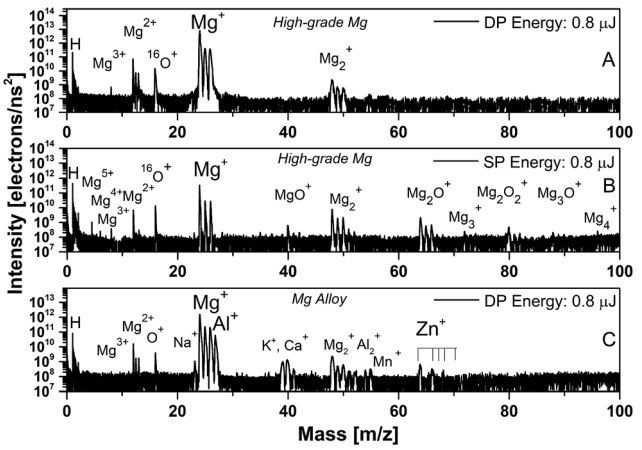

Fig. 9 Comparison between the mass spectra obtained with the SP and DP ablation of a high-grade Mg sample (panels A & B) and DP ablation of a Mg alloy AZ31 (Goodfellow) sample (panel C) applying an inter-pulse delay of +20 ps and a similar total pulse energy of 0.8 μJ.

delay of +20 ps. The SP spectra also show, in addition to isotope mass peaks of Mg^+, a number of Mg_x^+ clusters and Mg_xO_y oxides, where $x = 1$ to 4 and $y = 1$ to 3. In the SP mass spectrum the multiple-charged Mg^{n+} and O^{m+} ions with $n = 1$–5 and $m = 1$–3 ions are measured whereas in the DP mass spectra only Mg^{2+} and Mg^{3+} ions are observed in addition to Mg^+ and Mg_2^+. The mass peak intensity of the Mg_2^+ cluster ion can be reduced further by applying larger pulse energies but at the expense of decreasing the mass resolution.

The mass peaks of the DP spectrum are about 10 times more intense compared to the corresponding SP Mg^+ mass peaks. The mass peaks in the DP spectrum are observed to be broader, which is attributed to space charge effects due to larger amounts of ions produced during DP ablation (*e.g.*, coulombic repulsion). Observation of atomic ions of charges up to 5 in SP ablation and only up to 3 in DP ablation is accounted for by an increase of multiple-charged ion production efficiency at the sample surface due to larger pulse energy applied for ablation in the SP method. Multiple-charged species are observed to be produced less efficiently in the DP method at the currently applied laser ablation energies. The DP mass spectra can be measured within about 6 decades of the detection range and mass resolution ($m/\Delta m$) close to 300 at mass $m = 64$.

The measurement of the DP mass spectra is repeated on an Mg alloy. Again, no other clusters but only Mg_2^+ cluster is measured. In this case, the direct measurement of the Zn^+ ion in the Mg alloy can be made unambiguously. By applying the SP method alone, the presence of Mg_2O^+ clusters would make the identification of the minor element Zn more difficult. The absence of the Mg_2O^+ ion cluster simplifies elemental and isotope analysis and enables straightforward compositional analysis of the alloy sample. The measurement is in good agreement with the elemental composition given by Goodfellow (Mg: 96%, Al: 3% and Zn: 1%). We have also observed the mass peak with the mass $m = 55$ which is assigned to the Mn^+ ion and is not given in the specification sheet by Goodfellow. Additionally, Na^+, K^+, and Ca^+ ions were detected and are likely due to contamination introduced by the attachment of the Mg alloy sample to the sample holder. The current measurements are conducted using just one detection channel of our high-speed microstrip multi-anode multichannel plate detector system. In that measurement mode a detection limit of about 1–10 ppm can be achieved. The current detection limitation is due to the presence of underlying noise levels (cross talking). Better shielding efficiency and implementation of currently available 12 bit acquisition cards will help in further improvements of our detection limits while using one detection channel.

Discussion

The mass spectrometric analyses of the plasmas produced by SP and DP ablations deliver means to define optimal conditions for the atomic ion signal enhancement and reduction of cluster abundances in the analysed ion beam. Moreover, from the combined SP and DP chemical analyses one can also achieve sensitive diagnostics of the physical and chemical conditions of the plasma including an insight into the ablation mechanism and atomic/cluster ion formation processes. This is achieved by probing the plasma composition (produced by the first laser pulse) using the second laser pulse at different inter-pulse delays. In this method the DP ion yield is a measure of the coupling strength of the second pulse with the evolved plasma.

Our studies conducted with the DP method are in good agreement with the proposed DP ablation mechanism. By measuring the Mg^+ ion yield as a function of inter-pulse delay, we can follow the coupling strength of the delayed pulse with the dynamics of the produced plasma.[7] For the laser pulse energies below AET, negligible concentrations of the Mg^+ ions are observed for closely overlapping pulses. Neither the individual pulse energies nor the sum of energies of the individual pulses exceeds AET under these conditions (Fig. 3 and 4; see also discussion on the effects due to surface preconditioning and laser interference effects). Also for nearly overlapped laser

Published on 18 May 2018. Downloaded on 8/13/2018 3:18:34 PM.

pulses (inter-pulse delays: ~1 ps) the Mg^+ ion yield is negligible but it increases when the second pulse is applied within the inter-pulse delay range from 1 to 35 ps. For these delays, the Mg^+ ion signal enhancement is consistent with the mechanism in which the ions are produced by the interaction of the second laser pulse with the predominately neutral gaseous material (see Fig. 4 for the lowest pulse energies). This "plasma ignition" resulted in a large increase of the atomic ion fraction of the plume occurring in a relatively narrow range of the inter-pulse delays; a fast increase of the Mg^+ ion signal in the inter-pulse delay range from 1 to 20 ps followed by its fast decay is observed and reaches a level of the SP Mg^+ ion signal for delays longer than 35 ps (Fig. 4 and 6). Following the method applied in ref. 7 we can estimate the density of energy at the ablated volume. This is in the order of 10^{10} to 10^{11} J m^{-3} assuming the optical penetration depth of 10 nm, the incident laser fluence of 0.2 J cm^{-2} and the surface reflectance of $R = 0.5$. The electron temperature and electron phonon time coupling constant can be estimated roughly to be close to $T_e \approx 8000$ K and $\tau_{e-ph} \approx 10$ ps, respectively. This is consistent with the Mg^+ ion yield rise times. The Mg^+ ion yield maximum is observed already at the inter-pulse delays close to 20 ps and it is within the inter-pulse delay measurement accuracy independent of the applied pulse energies (Fig. 4–6). Hence, the measurement results are consistent with the estimated electron phonon coupling constant, τ_{e-ph}, and indicate a fast increase of lattice temperature and melting in the irradiated layer for pulse energies close to and above AET. In fact, the energy density is sufficiently high 10^{10} to 10^{11} J m^{-3} which shows that the lattice temperature can rise above the melting point. For pulse energies larger than ~0.5 μJ the Mg^+ ion signal enhancement rate is observed to decrease slower and eventually reaches the level of the SP Mg^+ ion signal for the inter-pulse delays larger than 300 ps. This can be qualitatively observed in Fig. 6 when the pulses of different energies are applied. In this case cooling dynamics of the molten layer takes a longer time. The changes of the Mg^+ ion yield as a function of pulse energy are somewhat different from that observed for the Co^+ ion yield in the ablation of Co/ZnS targets where for low laser energy densities slow melting times and slow cooling dynamics for much longer times were observed.[7] Our results are consistent with homogeneous ablation dynamics.

With an increase of the ablation pulse energy a denser plasma plume is produced. Partially ionised atomic vapour in the plume increases the absorption of laser radiation compared to that of the sample surface by means of the bound–bound and bound–free transitions enhanced by Stark broadening. This mechanism is proposed to be the main ionisation mechanism at the inter-pulse delays up to a few hundred ps.[27,39] The absorbed laser radiation contributes to an increase of the plasma plume temperature. We observe for pulse energies above AET an increase of the Mg^{2+} and Mg^{4+} ion concentrations in the inter-pulse delay range from 1 to 50 ps and 10 to 30 ps, respectively. This effect can be correlated with an increase of the efficiency of the ion production with an increase of the plume temperature (Fig. 5 and 7). The effect of the plasma formation and pulse energy dependence on the atomic ion formation are exemplified in DP ablation by different pulse energies for the first and second pulse (Fig. 6). For the total pulse energy being similar, Mg^+ ion production is more efficient when the energy of the second delayed pulse is larger. The maximum of the Mg^{2+} yield is measured for a similar inter-pulse delay of ~20 ps at which also the Mg^+ yield is maximal and is likely that at this delay the plasma temperature is highest.

The combined SP and DP ablation mass spectrometric analyses of the Mg cluster ion signals deliver an insight into the cluster formation mechanism. In DP ablation the production of clusters depends critically on absorbed laser energy (Fig. 7). The rise of the Mg_2^+ cluster ion signal observed in the delay range 1 to 30 ps for the pulse energies lower than 0.5 μJ is accounted for by favourable plasma conditions (sufficiently low plasma temperature and sufficiently high plasma density for neutral-charged reactions). A decomposition of the Mg_2^+ and other clusters can be observed for the pulse energies larger than 0.6 μJ. A minimal Mg_2^+ cluster ion yield is observed again for the inter-pulse delay close to 20 ps at which the Mg^+ ion yield is maximised and the plasma temperature is highest (Fig. 5). Due to a short inter-pulse delay it is likely that at least a fraction of the Mg_2^+ clusters is formed at the sample surface and eventually these clusters undergo decomposition in the plasma plume heated to sufficiently high temperature by the second pulse.

Efficient Mg cluster production is observed using the SP method in the range of the pulse energies applied. The observation of Mg_x^+ clusters and $Mg_xO_y^+$ oxides points towards the post-plasma chemistry mechanism involving neutral-ion reactions.[76,77] Our measurements indicate that in DP ablation the neutral-ion reactions occurring typically during the plasma expansion and cooling stages are less efficient. This is likely due to the low density of neutral atoms (ionisation by the second laser pulse) and an increased plasma temperature (heating the plasma by the second laser pulse).

Our analyses of the Mg^+ ion signal indicate that the enhancement of the Mg^+ ion concentrations by DP ablation compared to SP ablation occurs in the limited pulse energy range from 0.2 to ~1 μJ (Fig. 8). For pulse energies larger than 0.8 μJ the plasma density can be sufficiently high that plasma shielding effects can start to play the role and the laser pulse can interact with the uppermost thin layer in the plasma plume with reduced efficiency to heat the plasma to high temperature or efficiently ionise the neutral fraction.

The mass spectrometric analyses conducted with the DP ablation ion source indicate that this source can be promising in delivering enhanced atomic ion yields at reduced cluster ion yields. This is of considerable interest while conducting quantitative chemical analysis by mass spectrometry and will allow us to improve signal-to-noise ratios, detection sensitivity and reduce isobaric interference due to the presence of cluster ions. Although the performance of the source to deliver stoichiometric atomic ion fractions was not fully explored in the present investigations first results on a high purity Mg foil and Mg alloy indicate no ion source fractionation effects either in the measurements of isotopes or elemental composition. Also the multiply-charged ion production rate is reduced here compared to that observed in SP ablation of the same pulse energy, which

 This journal is © The Royal Society of Chemistry 2018

Published on 18 May 2018. Downloaded on 8/13/2018 3:18:34 PM.

again is advantageous for the quantitative chemical analysis.[78] The mass spectrometric analysis of the DP ablation products including atomic ions, multiply charged ions and cluster ions proves to be a powerful method complementing other plasma diagnostic methods and further mass spectrometric investigations with a more advanced pulse-shaping method may allow more advanced control over both the physical plasma conditions and chemical reactions.[7,8,37,39,79–81]

Summary

Mass spectrometric studies of the Mg plasma produced by DP femtosecond laser ablation/ionisation on an Mg foil are conducted using a miniature time-of-flight mass spectrometer. The positively charged Mg^+, multiply-charged Mg and Mg cluster ion yields are analysed as a function of the inter-pulse delay and the laser pulse energy. The results of these studies define optimal inter-pulse delay and pulse energy ranges at which the Mg^+ ion yield can be maximised and the interference due to Mg cluster ions is minimised. We find an enhancement of Mg^+ ion production by a factor of 20 in the inter-pulse delay range from 2 to 30 ps and in the pulse energy range from 0.2 to ~1.0 μJ compared to SP ablation with similar pulse energy. Although for larger pulse energies the Mg^+ ion yields become similar for SP and DP methods, DP ablation is advantageous allowing a significant reduction of the clusters in the plasma plume.

Furthermore, our studies show that the chemical analysis of solids can be conducted at relatively low pulse energies. Such energy levels can be produced by today's small-size fibre lasers. With up to a few μJ laser pulse energy and laser focusing down to a few μm measurement conditions can be achieved which allow conducting quantitative chemical analyses of any material including metals, isolators or semiconductors by using our LIMS system. Coupling the DP ion source with our miniature time-of-flight mass spectrometer can open new perspectives for *in situ* analysis of solids on planetary surfaces. Detection limits of our LIMS system are determined at a few ppb levels (with our high-speed microstrip multi-anode multichannel plate detector system).[72] The current improvements help in increase of the signal-to-noise ratio (SNR) but it will be particularly helpful to reduce the cluster concentrations and to improve the identification of trace and ultra-trace elements. The apparent complexity of the optical setup can be reduced by application of a small-size fibre laser system. This can be advantageous for application in space research, on a lander or rover, where space, weight and power consumption are limited.

Conflicts of interest

There are no conflicts to declare.

Acknowledgements

This work is supported by the Swiss National Science Foundation Project No. 172488. The authors acknowledge support of Prof. T. Feurer in this project.

References

1 E. Millon, O. Albert, J. C. Loulergue, J. Etchepare, D. Hulin, W. Seiler and J. Perriere, *J. Appl. Phys.*, 2000, **88**, 6937–6939.
2 R. R. Gattass and E. Mazur, *Nat. Photonics*, 2008, **2**, 219–225.
3 C. A. Hartmann, T. Fehr, M. Brajdic and A. Gillner, *J. Laser Micro/Nanoeng.*, 2007, **2**, 44–48.
4 B. Tan and K. Venkatakrishnan, *Opt. Express*, 2009, **17**, 1064–1069.
5 B. C. Windom and D. W. Hahn, *J. Anal. At. Spectrom.*, 2009, **24**, 1665–1675.
6 S. A. Fernandes, B. Schoeps, K. Kowalick, R. Nett, C. Esen, M. Pickshaus and A. Ostendorf, *Phys. Procedia*, 2013, **41**, 795–802.
7 I. Lopez-Quintas, V. Loriot, D. Avila, J. G. Izquierdo, E. Rebollar, L. Banares, M. Castillejo, R. de Nalda and M. Martin, *Phys. Chem. Chem. Phys.*, 2016, **18**, 3522–3529.
8 T. A. Labutin, V. N. Lednev, A. A. Ilyin and A. M. Popov, *J. Anal. At. Spectrom.*, 2016, **31**, 90–118.
9 J. Pisonero and D. Gunther, *Mass Spectrom. Rev.*, 2008, **27**, 609–623.
10 F. Poitrasson and F. X. d'Abzac, *J. Anal. At. Spectrom.*, 2017, **32**, 1075–1091.
11 B. C. Zhang, M. H. He, W. Hang and B. L. Huang, *Anal. Chem.*, 2013, **85**, 4507–4511.
12 A. Riedo, M. Neuland, S. Meyer, M. Tulej and P. Wurz, *J. Anal. At. Spectrom.*, 2013, **28**, 1256–1269.
13 R. E. Russo, X. L. Mao, C. Liu and J. Gonzalez, *J. Anal. At. Spectrom.*, 2004, **19**, 1084–1089.
14 S. Nolte, C. Momma, H. Jacobs, A. Tunnermann, B. N. Chichkov, B. Wellegehausen and H. Welling, *J. Opt. Soc. Am. B*, 1997, **14**, 2716–2722.
15 V. Zorba, X. L. Mao and R. E. Russo, *Anal. Bioanal. Chem.*, 2010, **396**, 173–180.
16 S. S. Wellershoff, J. Hohlfeld, J. Gudde and E. Matthias, *Appl. Phys. A: Mater. Sci. Process.*, 1999, **69**, S99–S107.
17 E. G. Gamaly and A. V. Rode, *Prog. Quantum Electron.*, 2013, **37**, 215–323.
18 T. Kramer, B. Neuenschwander, B. Jaggi, S. Remund, U. Hunziker and J. Zurcher, *Laser Assisted Net Shape Engineering 9 International Conference on Photonic Technologies Proceedings of the Lane 2016*, 2016, 83, pp. 123–134.
19 L. V. Zhigilei, *Appl. Phys. A: Mater. Sci. Process.*, 2003, **76**, 339–350.
20 D. Scuderi, O. Albert, D. Moreau, P. P. Pronko and J. Etchepare, *Appl. Phys. Lett.*, 2005, **86**, 071502.
21 R. Le Harzic, D. Breitling, S. Sommer, C. Fohl, K. Konig, F. Dausinger and E. Audouard, *Appl. Phys. A: Mater. Sci. Process.*, 2005, **81**, 1121–1125.
22 X. Zhao and Y. C. Shin, *Appl. Phys. B: Lasers Opt.*, 2015, **120**, 81–87.
23 A. Semerok and C. Dutouquet, *Thin Solid Films*, 2004, **453**, 501–505.
24 V. Pinon, C. Fotakis, G. Nikolas and D. Anglos, *Spectrochim. Acta, Part B*, 2008, **63**, 1006–1010.
25 A. Semerok and P. Mauchien, *Rev. Laser Eng.*, 2005, **38**, 530–535.

Published on 18 May 2018. Downloaded on 8/13/2018 3:18:34 PM.

26 S. Amoruso, R. Bruzzese, X. Wang, G. O'Connell and J. G. Lunney, *J. Appl. Phys.*, 2010, **108**, 113302.
27 T. Donnelly, J. G. Lunney, S. Amoruso, R. Bruzzese, X. Wang and X. Ni, *J. Appl. Phys.*, 2009, **106**, 013304.
28 S. Noel and J. Hermann, *Appl. Phys. Lett.*, 2009, **94**, 053120.
29 R. Stoian, A. Mermillod-Blondin, N. M. Bulgakova, A. Rosenfeld, I. V. Hertel, M. Spyridaki, E. Koudoumas, P. Tzanetakis and C. Fotakis, *Appl. Phys. Lett.*, 2005, **87**, 124105.
30 I. M. Burakov, N. M. Bulgakova, R. Stoian, A. Rosenfeld and I. V. Hertel, *Appl. Phys. A: Mater. Sci. Process.*, 2005, **81**, 1639–1645.
31 J. Mildner, C. Sarpe, N. Gotte, M. Wollenhaupt and T. Baumert, *Appl. Surf. Sci.*, 2014, **302**, 291–298.
32 M. E. Povarnitsyn, T. E. Itina, P. R. Levashov and K. V. Khishchenko, *Appl. Surf. Sci.*, 2011, **257**, 5168–5171.
33 N. M. Bulgakova, A. V. Bulgakov and O. F. Bobrenok, *Phys. Rev. E: Stat., Nonlinear, Soft Matter Phys.*, 2000, **62**, 5624–5635.
34 A. Brantov, W. Rozmus, R. Sydora, C. E. Capjack, V. Y. Bychenkov and V. T. Tikhonchuk, *Phys. Plasmas*, 2003, **10**, 3385–3396.
35 T. E. Itina, F. Vidal, P. Delaporte and M. Sentis, *Appl. Phys. A: Mater. Sci. Process.*, 2004, **79**, 1089–1092.
36 J. K. Chen and J. E. Beraun, *J. Opt. A: Pure Appl. Opt.*, 2003, **5**, 168–173.
37 M. E. Povarnitsyn, T. E. Itina, M. Sentis, K. V. Khishchenko and P. R. Levashov, *Phys. Rev. B: Condens. Matter Mater. Phys.*, 2007, **75**, 235414.
38 S. Amoruso, R. Bruzzese, X. Wang and J. Xia, *Appl. Phys. Lett.*, 2008, **93**, 191504.
39 T. Donnelly, J. G. Lunney, S. Amoruso, R. Bruzzese, X. Wang and X. Ni, *J. Appl. Phys.*, 2010, **108**, 043309.
40 M. E. Povarnitsyn, N. E. Andreev, P. R. Levashov, K. V. Khishchenko and O. N. Rosmej, *Phys. Plasmas*, 2012, **19**, 023110.
41 M. E. Povarnitsyn, N. E. Andreev, E. M. Apfelbaum, T. E. Itina, K. V. Khishchenko, O. F. Kostenko, P. R. Levashov and M. E. Veysman, *Appl. Surf. Sci.*, 2012, **258**, 9480–9483.
42 M. E. Povarnitsyn, V. B. Fokin and P. R. Levashov, *Appl. Surf. Sci.*, 2015, **357**, 1150–1156.
43 M. E. Povarnitsyn, V. B. Fokin, P. R. Levashov and T. E. Itina, *Phys. Rev. B: Condens. Matter Mater. Phys.*, 2015, **92**, 174104.
44 S. Amoruso, R. Bruzzese, X. Wang and J. Xia, *Appl. Phys. Lett.*, 2008, **92**, 041503.
45 P. A. Atanasov, N. N. Nedialkov, S. Amoruso, R. Bruzzese and X. Wang, *C. R. Acad. Bulg. Sci.*, 2008, **61**, 863–870.
46 X. Zhao and Y. C. Shin, *Appl. Phys. Lett.*, 2014, **105**, 111907.
47 S. I. Ashitkov, S. A. Romashevskii, P. S. Komarov, A. A. Burmistrov, V. V. Zhakhovskii, N. A. Inogamov and M. B. Agranat, *Quantum Electron.*, 2015, **45**, 547–550.
48 S. Amoruso, X. Wang, C. Altucci, C. de Lisio, M. Armenante, R. Bruzzese, N. Spinelli and R. Velotta, *Appl. Surf. Sci.*, 2002, **186**, 358–363.
49 S. Amoruso, X. Wang, C. Altucci, C. de Lisio, M. Armenante, R. Bruzzese and R. Velotta, *Appl. Phys. Lett.*, 2000, **77**, 3728–3730.
50 Z. Zhang, P. A. VanRompay, J. A. Nees and P. P. Pronko, *J. Appl. Phys.*, 2002, **92**, 2867–2874.
51 M. E. Povarnitsyn, T. E. Itina, K. V. Khishchenko and P. R. Levashov, *Phys. Rev. Lett.*, 2009, **103**, 195002.
52 R. Stoian, M. Boyle, A. Thoss, A. Rosenfeld, D. Ashkenasi, G. Korn, E. E. B. Campbell and I. V. Hertel, *Second International Symposium on Laser Precision Microfabrication*, 2002, 4426, pp. 78–81.
53 R. Stoian, N. M. Bulgakova, A. Mermillod-Blondin, A. Rosenfeld, M. Spyridaki, E. Koudoumas, C. Fotakis and I. V. Hertel, *Ultrafast Phenomena in Semiconductors and Nanostructure Materials Ix*, 2005, 5725, pp. 329–343.
54 U. Rohner, J. A. Whitby and P. Wurz, *Meas. Sci. Technol.*, 2003, **14**, 2159–2164.
55 P. Wurz, D. Abplanalp, M. Tulej, M. Iakovleva, V. A. Fernandes, A. Chumikov and G. G. Managadze, *Sol. Syst. Res.*, 2012, **46**, 408–422.
56 P. Wurz, D. Abplanalp, M. Tulej and H. Lammer, *Planet. Space Sci.*, 2012, **74**, 264–269.
57 M. B. Neuland, S. Meyer, K. Mezger, A. Riedo, M. Tulej and P. Wurz, *Planet. Space Sci.*, 2014, **101**, 196–209.
58 A. Riedo, S. Meyer, B. Heredia, M. B. Neuland, A. Bieler, M. Tulej, I. Leya, M. Iakovleva, K. Mezger and P. Wurz, *Planet. Space Sci.*, 2013, **87**, 1–13.
59 M. Tulej, A. Riedo, M. B. Neuland, S. Meyer, P. Wurz, N. Thomas, V. Grimaudo, P. Moreno-Garcia, P. Broekmann, A. Neubeck and M. Ivarsson, *Geostand. Geoanal. Res.*, 2014, **38**, 441–466.
60 M. Tulej, A. Neubeck, M. Ivarsson, A. Riedo, M. B. Neuland, S. Meyer and P. Wurz, *Astrobiology*, 2015, **15**, 669–682.
61 A. Neubeck, M. Tulej, M. Ivarsson, C. Broman, A. Riedo, S. McMahon, P. Wurz and S. Bengtson, *Int. J. Astrobiol.*, 2016, **15**, 133–146.
62 A. A. Sysoev and A. A. Sysoev, *Eur. J. Mass Spectrom.*, 2002, **8**, 213–232.
63 Q. Yu, L. Z. Chen, R. F. Huang, W. Hang, J. He and B. L. Huang, *TrAC, Trends Anal. Chem.*, 2009, **28**, 1174–1185.
64 Y. M. Lin, R. B. Xu, L. F. Li, W. Hang, J. He and B. L. Huang, *J. Anal. At. Spectrom.*, 2011, **26**, 1183–1190.
65 G. G. Managadze, P. Wurz, R. Z. Sagdeev, A. E. Chumikov, M. Tuley, M. Yakovleva, N. G. Managadze and A. L. Bondarenko, *Sol. Syst. Res.*, 2010, **44**, 376–384.
66 Y. M. Lin, Q. A. Yu, W. Hang and B. L. Huang, *Spectrochim. Acta, Part B*, 2010, **65**, 871–883.
67 J. He, R. F. Huang, Q. Yu, W. Hang and B. L. Huang, *Chem. J. Chin. Univ.*, 2009, **30**, 57–59.
68 R. Urs, A. W. James and W. Peter, *Meas. Sci. Technol.*, 2003, **14**, 2159.
69 A. Riedo, A. Bieler, M. Neuland, M. Tulej and P. Wurz, *J. Mass Spectrom.*, 2013, **48**, 1–15.
70 M. Tulej, M. Iakovleva, I. Leya and P. Wurz, *Anal. Bioanal. Chem.*, 2011, **399**, 2185–2200.
71 R. Wiesendanger, V. Grimaudo, P. Moreno, A. Cedeño López, A. Riedo, M. Tulej, A. Neubeck, M. Ivarsson, D. Wacey, H. Shea and P. Wurz, *Astrobiology*, 2018, DOI: 10.1089/ast.2017.1780.

 This journal is © The Royal Society of Chemistry 2018

72 A. Riedo, M. Tulej, U. Rohner and P. Wurz, *Rev. Sci. Instrum.*, 2017, **88**, 045114.
73 S. Meyer, A. Riedo, M. B. Neuland, M. Tulej and P. Wurz, *J. Mass Spectrom.*, 2017, **52**, 580–590.
74 T. Donnelly, J. G. Lunney, S. Amoruso, R. Bruzzese and X. Wang, *AIP Conf. Proc.*, 2010, **1278**, 643–655.
75 J. Bonse, S. Hohm, S. V. Kirner, A. Rosenfeld and J. Kruger, *IEEE J. Sel. Top. Quantum Electron.*, 2017, **23**, 9000615.
76 H. M. Hou, X. L. Mao, V. Zorba and R. E. Russo, *Anal. Chem.*, 2017, **89**, 7750–7757.
77 L. Liu, L. M. Deng, L. S. Fan, X. Huang, Y. Lu, X. K. Shen, L. Jiang, J. F. Silvain and Y. F. Lu, *Opt. Express*, 2017, **25**, 27000–27007.
78 V. V. Milyaeva, E. E. Sil'nikov, A. M. Mikhailov and A. A. Sysoev, *Eur. J. Mass Spectrom.*, 2017, **23**, 167–173.
79 C. R. Cheng and X. F. Xu, *Phys. Rev. B: Condens. Matter Mater. Phys.*, 2005, **72**.
80 S. Amoruso, R. Bruzzese, X. Wang, N. N. Nedialkov and P. A. Atanasov, *J. Phys. D: Appl. Phys.*, 2007, **40**, 331–340.
81 D. Perez and L. J. Lewis, *Phys. Rev. B: Condens. Matter Mater. Phys.*, 2003, **67**, 184102.

Published on 18 May 2018. Downloaded on 8/13/2018 3:18:34 PM.